Universiteit Antwerpen

This item is the archived peer-reviewed author-version of:

A facile synthesis of Ag@PdAg core-shell architecture for efficient purification of ethene feedstock

Reference:
Ma Rui, He Yufei, Feng Junting, Hu Zhi-Yi, Van Tendeloo Gustaaf, Li Dianqing.- A facile synthesis of Ag@PdAg core-shell architecture for efficient purification of ethene feedstock
Journal of catalysis - ISSN 1090-2694 - 369(2019), p. 440-449
Full text (Publisher's DOI): https://doi.org/10.1016/J.JCAT.2018.11.037
To cite this reference: https://hdl.handle.net/10067/1812610151162165141

uantwerpen.be
Institutional repository IRUA

A facile synthesis of Ag@PdAg core-shell architecture for efficient purification of ethene feedstock

Rui Ma,[a,b] Yufei He,[*a,b] Junting Feng,[a,b] Zhi-Yi Hu,[*c,d,e] Gustaaf Van Tendeloo,[c,e] Dianqing Li [*a,b]

a. Address here. State Key Laboratory of Chemical Engineering, Beijing University of Chemical Technology, Beijing, 100029 (P.R. China)

b. Beijing Engineering Center for Hierarchical Catalysts, Beijing University of Chemical Technology, Beijing, 100029 (P.R. China)

c. Wuhan University of Technology, Wuhan, 122 Luoshi Road, 430074 (P.R. China)

d. State Key Laboratory of Advanced Technology for Materials Synthesis and Processing, Wuhan University of Technology, Wuhan, 122 Luoshi Road, 430074 (P.R. China)

e. EMAT (Electron Microscopy for Materials Science), University of Antwerp Groenenborgerlaan 171, B-2020 Antwerp (Belgium)

* Corresponding author

E-mail address: yfhe@mail.buct.edu.cn (Y. F. He), lidq@mail.buct.edu.cn (D. Q. Li), Zhiyi.hu@whut.edu.cn (Z. Y. Hu)

Abstract

Precise control of elemental configurations within multimetallic nanoparticles could enable access to functional nanomaterials with significant performance benefits. Here, we present a one-pot synthesis of supported Ag@PdAg core-shell catalyst with an ordered PdAg alloy shell and an Ag core. Both the relative reduction potential and ratio of metal precursors are essential for this synthesis strategy. The distinguished properties of Ag@PdAg, particularly the electronic structure, indicates the existence of electron modification not only between Pd and Ag on PdAg shell, but between Ag core and alloy shell. The Ag@PdAg catalyst displays 97% ethene yield in the partial hydrogenation of acetylene, which is 2.0 and 8.1 times that of over PdAg alloy and pure Pd catalysts, and this is the most selective catalyst reported to data under industrial evaluation conditions. Moreover, this core-shell structure exhibits preferable stability with comparison to PdAg alloy catalyst. The facile synthesis of core-shell architecture with alloy shell structure provides a new platform for efficient catalytic transfer of chemical resource.

Keywords:

Bimetallic catalysts; Ag@PdAg core-shell; Selective hydrogenation of acetylene; Electron modification.

1 Introduction

The design of high performance catalysts is the main driving force in the critical field of heterogeneous catalysis, which is the foundation of chemical industry [1-5]. Bimetallic materials, due to their electronic and chemical properties that are distinct from those of their parent metals, offer the opportunity to obtain excellent catalysts with enhanced selectivity, activity and stability [6-9]. In recent years, core-shell architecture, particularly composed of noble metals including Au, Ag, Pt, and Pd have attracted extensive research interest due to its unique properties [10-14]. For example, Koenigsmann et al. [15] revealed the existence of change in the surface d-band center of Pt shell due to lattice distortion in Pd@Pt core-shell nanoparticles, which showed superior activity than Pt/C catalyst in oxygen reduction reaction. Tsang's group [16] found a charge transfer between shell and core in Ag@Pd core-shell nanostructure which can significantly enhance the production of H_2 from formic acid. These peculiarities originated from the construction of core-shell architecture enable them to exhibit superior performance in the fuel-cell electrocatalysis, energy storage materials, enhanced optical devices and many important catalytic processes [17-21]. In addition, the fabrication of core-shell architecture is also a promising strategy with significant economic advantages because it could maximize the precious element's surface to volume ratio, especially for the efficient usage of noble metals. Considering that heterogenous catalysis is performed on the surface of a catalyst, even with the merit of the M@N bimetallic core-shell materials (M and N represent a metal), the monometallic surface will still limit the applications of this materials [22-24]. Bimetallic alloy nanostructures, which generally introduce the electronic and geometric effect, will overcome the limitation of the monometallic surface in M@N structure by

the fabrication of surface alloy M@MN core-shell architecture, and also bring new characters that may help improve the performance of heterogeneous catalyst, even under a harsh condition [1,4,25-27]. Therefore, the investigations on the synthesis and application of surface alloy core-shell NPs is of great interest for harvesting the combined advantages of synergistic structural/electronic effects of core-shell structure and the intrinsic property of the alloy structure.

Lots of efforts have been devoted to explore the facile methods to synthesize surface alloy core-shell morphologies. To the best of our knowledge, only several core-shell architectures such as Pd@FePt, Pd@AuCu and Au@Ni_mPt_2 have been successfully prepared using the epitaxial growth method which is carried out in the presence of seeds and surfactant [28-30]. However, the nanocrystals obtained from this method have inherent limitations associated with the ligand covered surfaces, which not only limit the free access of surface active sites but hinder electron transport between the catalyst and the support and then deteriorate the catalytic performance [31,32]. Moreover, the reported M@MN core-shell architecture possessed a noble metal core structure, resulting in the waste of precious resources to some degree. One-pot synthesis strategy could provide an efficient approach to prepare supported bimetallic catalysts, however, this strategy usually produces a nanostructure with uncontrolled atom distribution. To obtain a desired bimetallic nanostructure using one-pot strategy, it is of significance to control the reduction process, such as the reduction potential of the metal precursor, the reduction medium, the ability of the reducing agents as well as the interaction between the reduced metal.

Herein, we present a facile one-pot approach to synthesize supported Ag@PdAg core-shell catalyst in N, N-dimethylformamide (both as solvent and reducing agent) solution without any seeds or surfactants on MgAl layered double hydroxide. During the reduction process, both the reduction potential and ratio of metal precursors are crucial for the formation of Ag@PdAg core-shell nanostructure. The obtained core-shell catalyst could specifically hydrogenate acetylene in an ethene-rich stream, which showed superior catalytic performance with comparison to PdAg alloy catalyst with same surface composition, even at the ppm level of acetylene. Moreover, it also

exhibited preferable stability compared to PdAg alloy catalyst in a continuous run. We note that 97% ethene yield was obtained over this Ag@PdAg core-shell catalyst at almost completed acetylene conversion, which is the most selective catalyst for the selective hydrogenation of acetylene under the industrial evaluation conditions.

2 Experimental

2.1 Materials

$PdCl_2$, $AgNO_3$, $Pd(acac)_2$, poly(vinyl pyrrolidone) (PVP, MW = 40000), $NaBH_4$, and N, N-dimethylformamide (DMF, chromatographically pure) were purchased from Sigma-Aldrich Co. and used without further purification.

2.2.1 One-pot synthesis of supported Ag@PdAg catalyst

The entire synthesis of Ag@PdAg core-shell nanoparticles supported on Mg_2Al-LDH is quite simple and is accomplished by simultaneously reducing precursor of $Pd(acac)_2$ and $AgNO_3$ in the presence of support. The LDHs, a type of two-dimensional (2D) layered inorganic material offering several advantages as a catalyst support for hydrogenation reaction [33,34]—such as tunable basicity and acidity of the surface, the ability to incorporate a variety of cations in the brucite-like layers and high adsorption capacity for the immobilization of active species, was prepared by hydrothermal method and the procedures have been described in detail elsewhere [35]. In a typical one-pot synthesis of supported Ag@PdAg catalyst, $Pd(acac)_2$ (3.3 mg) and $AgNO_3$ (5.5 mg) were dissolved in 100 mL of DMF. After that, 0.5 g support was added into the mixed solution and the mixture was ultrasonicated for 5 min. The resulting homogeneous mixture was then heated at 140 ^oC in an oil bath under vigorous stirring conditions. After 1 h the suspension was cooled to room temperature, the catalyst washed thoroughly with ethanol and dried at 70 ^oC overnight.

2.2.2 Preparation of supported monometallic Pd, Ag, and PdAg alloy catalysts.

For comparison, PdAg alloy catalyst with molar ratio n(Pd) : n(Ag) = 2 was prepared by co-reduction of Na_2PdCl_4 and $AgNO_3$ using $NaBH_4$ in the presence of PVP. In

detailed, Na_2PdCl_4, $AgNO_3$ and $NaBH_4$ were dissolved in 100 mL deionized water (PVP/metal (wt./wt.) = 1.2, $NaBH_4$/metal (mol./mol.) = 5). The mixed solution was stirred at room temperature for 30 min, followed by the addition of 1g support. The amount of added metal was calculated to give a Pd loading of 1.0 wt.%. After an hour immobilization, the slurry was filtered, washed with deionized water and acetone several times and dried at 70 ºC overnight. In addition, supported Pd and Ag monometallic catalysts were also prepared by the same method.

2.3 Catalyst characterization

Transmission Electron Microscopy (TEM), High Angle Annular Dark Field Scanning Transmission Electron Microscopy (HAADF-STEM) and Energy Dispersive X-ray spectroscopy (EDX) were performed on a FEI Titan Themis microscope fitted with aberration-correctors for the probe forming lens and imaging lens, and a Super-X EDX system, operated at 300kV. Elemental analysis for Pd and Ag was performed using a Shimadzu ICPS-7500 inductively coupled plasma atomic emission spectrometer (ICP-AES). In situ diffuse reflectance infrared Fourier transform spectroscopy (DRIFTS) of CO chemisorption over catalysts were carried out on a Bruker Tensor 27 instrument under room temperature. XRD analysis of the Pd, Ag, and PdAg colloidal sols was performed on a Shimadzu XRD-6000 diffractometer using Cu Kα radiation (k = 0.154 nm) in the 2θ range of 35–70° with a scan speed of $10°\cdot Min^{-1}$. X-ray photoelectron spectra (XPS) of samples were recorded on a Thermo VGESCALAB 250 spectrometer equipped with Mg Kα anode. H_2 chemisorption was carried out on a Micrometric ChemiSorb 2920. The sample was maintained at 100 °C for 1 h in a pure Ar gas flow (40 cm^3/min), and then subjected to hydrogen chemisorption using a pulse titration (50 μL loop) procedure. The dispersion is determined on the assumption of a unity adsorption stoichiometry. C_2H_2 and C_2H_4-temperature-programmed desorption (TPD) of the catalysts was also conducted in this instrument, about 100 mg of fresh catalyst was preheated at 120 °C for 30 min in argon and then cooled to room temperature. The catalyst was then kept in a stream of ethene (acetylene) until the

adsorption was saturated, followed by treatment with helium for 30 min. Thermal analysis of coke deposition on used catalysts was performed on a TG/DTA X70 Thermogravimetric analyzer.

2.4 The selective hydrogenation of acetylene

The selective hydrogenation of acetylene was performed in a fixed-bed quartz microreactor with a space velocity (GHSV) of 10056 h^{-1} and relative pressure 0.4 MPa. Approximately 50 mg catalyst and 1.52g (1.0 mL) quartz sand were mixed and holded at the center of the 7 mm quartz tube. A mixed gas consisting of 32% C_2H_4 / 0.31% C_2H_2 / 0.6% H_2 / balance N_2 to give a H_2: C_2H_2 ratio of ~ 2:1. The gas composition from the microreactor outlet was analyzed by online gas chromatography equipped with a FID detector. At least five tests for each point were executed in order to obtain reproducible values and carbon balance determined from the effluent gas was 100±0.5%. Acetylene conversion, ethene selectivity, ethane selectivity and yield are defined as follows:

$$\text{Acetylene Conversion} = \frac{\text{Acetylene(inlet)} - \text{Acetylene(outlet)}}{\text{Acetylene(inlet)}}$$

$$\text{Ethene Selectivity} = \frac{\text{Ethene(outlet)} - \text{Ethene(inlet)}}{\text{Acetylene(inlet)} - \text{Acetylene(outlet)}}$$

$$\text{Ethane Selectivity} = \frac{\text{Ethane(outlet)} - \text{Ethane(inlet)}}{\text{Acetylene(inlet)} - \text{Acetylene(outlet)}}$$

$$\text{Yield} = \text{Conversion} \times \text{Selectivity}$$

3 Results and discussion

3.1 Structure and formation mechanism of supported Ag@PdAg catalyst.

The High Angle Annular Dark Field Scanning Transmission Electron Microscopy (HAADF-STEM) images (**Fig. 1**) show the morphology and structure of Ag@PdAg NPs distributed homogeneously on the LDHs substrate. The preparation method has little influence on the crystalline nature of LDHs support, more detailed information about LDHs of as-prepared Ag@PdAg/LDHs catalyst can be found in Fig S1 and Table S1. The size of Ag@PdAg NPs is mainly around 10-20 nm and the average size of Ag@PdAg nanoparticles is 15.5 nm (the particle size distribution showed in Fig. S2) with 85% particles within ±

3 nm size range. The corresponding Energy Dispersive X-ray spectroscopy (EDX) maps (Fig. 1d,e,f) of Ag and Pd present the Ag@AgPd core-shell structure of nanoparticles. In order to demonstrate the components on the shell, the High Resolution Scanning Transmission Electron Microscopy (HR-STEM) image (Fig. 1c and Fig. S3) shows an individual nanoparticle. The corresponding line profile of EDX signal (Fig. 1g) and EDX mapping results (Fig. S3 b,c,d) indicate the different counts intensities of Ag and Pd between the core and shell, which reveal that the AgPd alloy layer is on the surface of the nanoparticle with around 3 nm thickness. In addition, the high degree of crystallinity of Ag@PdAg NPs can be demonstrated by the HR-(S)TEM images (Fig. 1c and Fig. S4). Overall, the Ag@AgPd core-shell structure has been confirmed by (S)TEM and EDX results.

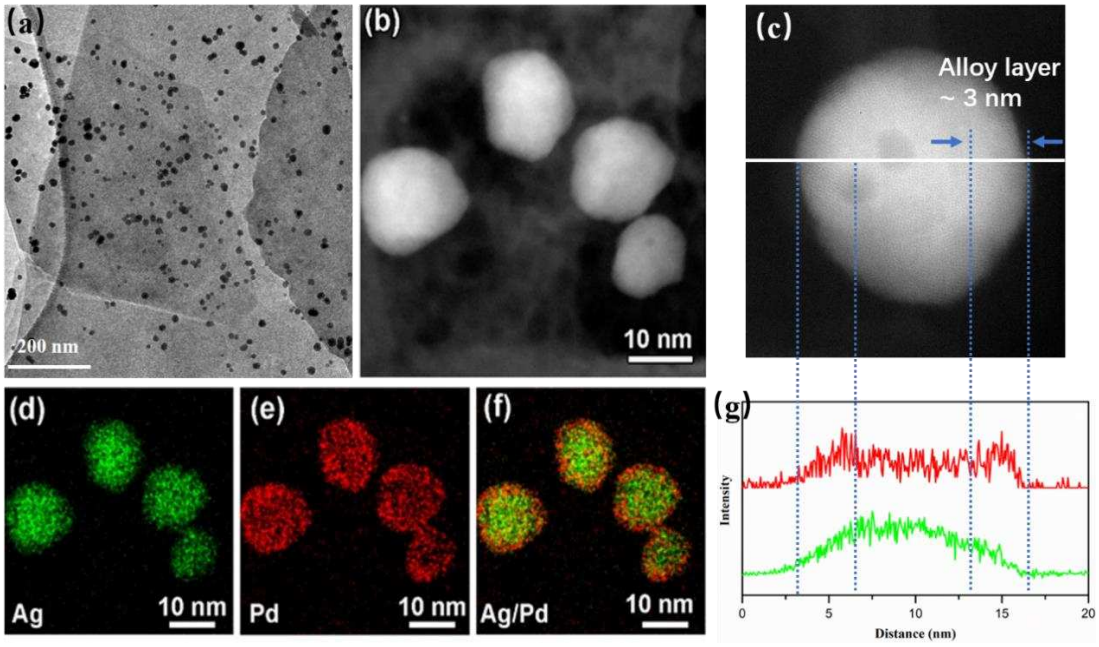

Fig. 1. (a) Low magnification TEM image, (b) high magnification HAADF-STEM image, (c) HRSTEM image of an individual nanoparticle, (g) corresponding EDX line scan indicated in (c) with the signals of Ag and Pd, (d-f) corresponding EDX elemental maps of the whole area in (b), Ag: green, Pd: red.

Rationally designed bimetallic core-shell nanostructure could not be easily synthesized without seeds. One-pot synthesis such as simultaneous reduction of

metallic precursors in the same reaction medium usually produced a bimetallic alloy. The detailed investigation on the formation mechanism of Ag@PdAg core-shell nanoparticles were performed on a series of STEM-EDX analysis (**Fig. 2**) by tracking the structure evolution during the core-shell crystal growth. Fig. 2 presents EDX elemental maps of three selected samples with different reaction time, (a) 20 minutes, (b) 30 minutes, and (c) 60 minutes, respectively. In 20 minutes reaction time sample, Ag NPs and a little Pd single atoms or clusters were formed, but no obvious core-shell structure can be observed in STEM-EDX (Fig. 2a). Nevertheless, the core-shell structure begins to form with around 2 nm thickness alloy shell after 30 minutes reaction time (Fig. 2b). When the reaction time extends to 50 minutes (Fig. 2c), the thickness of alloy shell could increase to around 3 nm. It implies that the thickness of the alloy shell can be tuned by the reaction time and a thin alloy shell starts formation after 20 minutes.

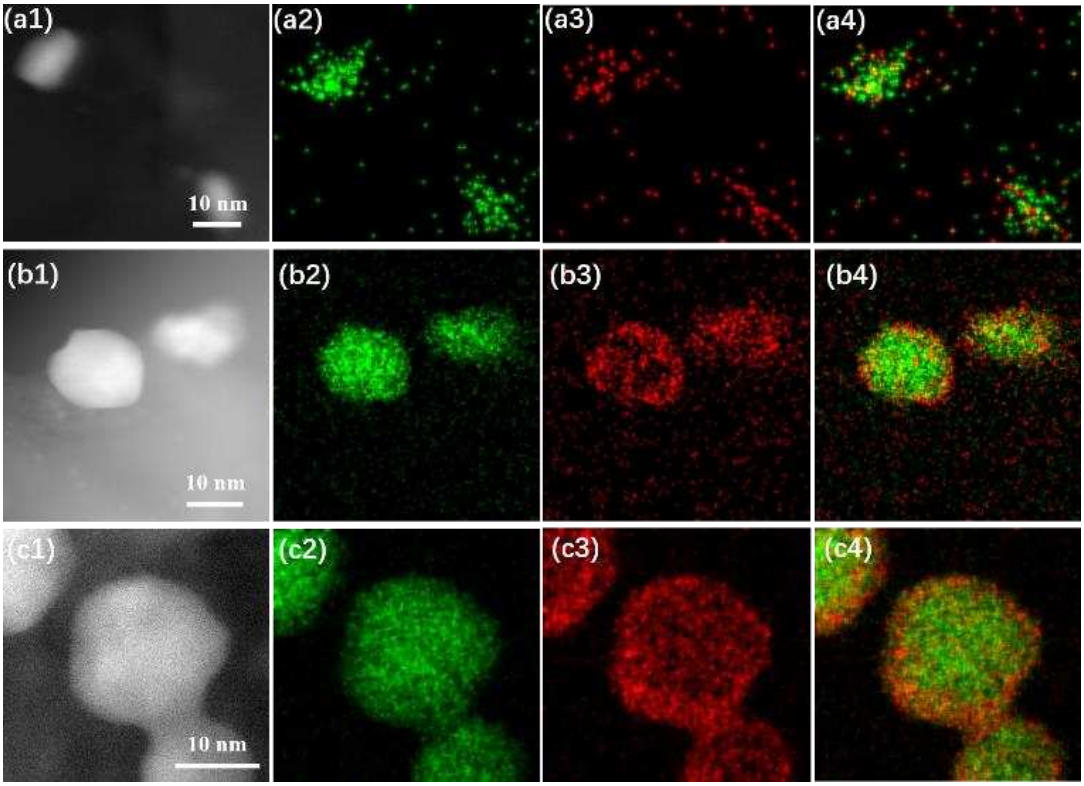

Fig. 2. (a-c) HAADF-STEM images with different reaction time (20, 30, and 60 minutes) and corresponding EDX elemental maps: Ag (green) and Pd (red).

Inductively Coupled Plasma-Atomic Emission Spectroscopy (ICP-AES) analysis was also taken to monitor the content of Ag and Pd at different reaction time. As showed in **Fig. 3**A, the deposition rate of Ag^{+} and Pd^{2+} can be divided into two regions. Within the first 10 min of reaction, the Ag loading (wt %) increased sharply from 0 to 0.32 %. In the second region between 10 and 40 min, the amount of Ag increased linearly with a rate of 0.011 % per min, which was much slower than that in the first region. After 40 min, the Ag content remains the same and the final Ag loading reached 0.66%. However, the reduction behavior of Pd^{2+} is quite different from Ag^{+}. In the initial stage, hardly any Pd atoms were detected until 20 min Pd^{2+} began to deposit. The ions in the solution are completely reduced and the reaction was finished after 40 min. Thus we can calculated that the PdAg ratio is 2:1 on the alloy shell. The rate of reduction of Pd is not constant, and the rate of deposition of Pd^{2+} starts slowly and then increases. The asynchronized reduction of Pd^{2+} and Ag^{+} in DMF system is according with the conclusions of STEM-EDX analysis. The distribution of Pd species in the obtained nanoparticle surface, which selected from different reaction time, was detected by Fourier Transform Infrared Spectroscopy (FTIR) via CO chemisorption. As showed in Fig. 3B, bands center range from 1900 to 2100 cm^{-1} were attributed to CO adsorbed on metallic Pd species [36-38]. The absence of any bounded CO on the surface of 20 min sample indicating there is no measurable Pd^{0}, which is consistent with the ICP-AES result. Three bands at 2052, 2027 and 1994 cm^{-1} were observed, suggesting Pd^{2+} was reduced with the extension of reaction time. In addition, the ratio of 2052 cm^{-1} band decrease, corresponding to the decrease of low coordination Pd atoms [39,40]. It suggests that long time reaction result in the formation of PdAg alloy, and the proportion of Pd is scaled-up with the increasing of shell thickness.

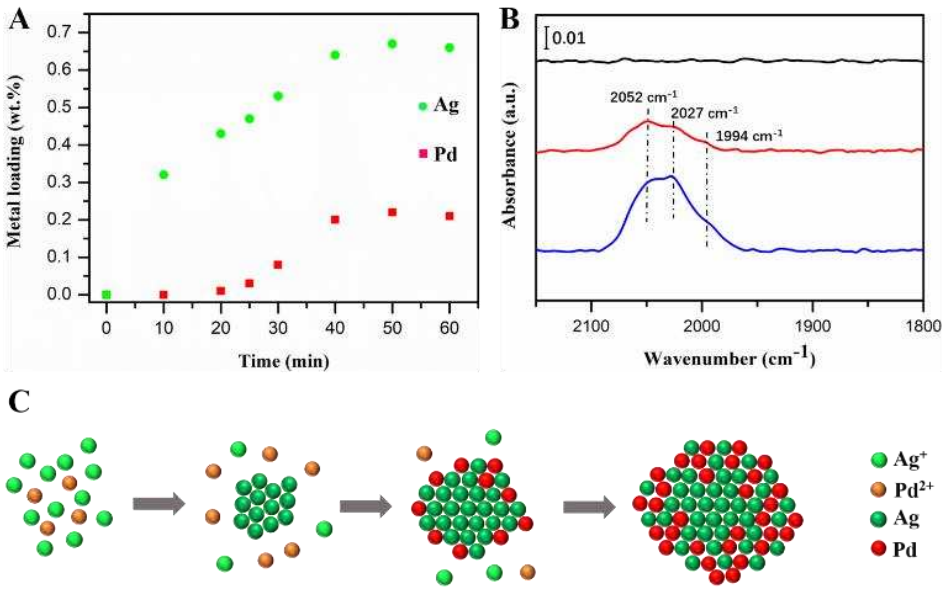

Fig. 3. (A) Metal loading (wt %) measured from ICP-AES of Ag@PdAg/LDHs at different reaction time, (B) CO-IR of obtained catalyst at 20, 30, 60 minutes reaction time, (C) formation schematic diagram of Ag@AgPd core-shell nanoparticle.

The differential of the relative reduction potential between two metal ions plays a crucial role in the formation of core-shell structure. When using DMF as reducing agent, we found evidence that the reduction of Ag^+ is more favorable than $Pd(acac)_2$ under 140 ^oC (Fig. S5). Moreover, the complete reduction time of Pd and Ag mixture is obviously reduced compared that of $Pd(acac)_2$, indicating the nucleated Ag could promotes the reduction of Pd in DMF (Fig. S6). A phenomenological growth procedure of Ag@PdAg is then proposed, as showed in Fig. 3C. In the initial stage, Ag^+ is preferentially reduced to form Ag nucleus. This process is driven by the difference reduction potentials between $AgNO_3$ and $Pd(acac)_2$. As the reaction goes on, abundant Pd^{2+} begin to catalytically reduce by the preformed Ag particles and deposit onto them, accompany with the reduction of the rest of Ag^+ in the solution. This process continues until all the metal precursor are completely consumed. We hold that the relative reduction potentials and ratio of metal precursors are the key factors for the formation of Ag@PdAg nanostructure. Besides, the concentration of two species has an important effect on the shell thickness and surface composition of the nanoparticles. For examples, we kept the concentration of Ag^+ constant and altered the mole of Pd^{2+}

(varies from 2mg, 3.3mg and 10mg to give a total Ag/Pd molar ratio of 5, 3 and 1, respectively) in the preparation system. As showed in Fig. 4, the nanostructure with Ag core and a PdAg alloy shell is barely changed. It could be observed that the size of Ag core is slightly less than 10 nm, while the thickness of PdAg alloy shell increases with the raising concentration of Pd precursor (from 0.5 nm to 5 nm). When Pd precursor content is further increased, a pure Pd shell would generate in outer of PdAg alloy layer owing to the full consumption of Ag precursor. XPS measurement (presented in Table S2) shows that the Ag/Pd atomic ratio in the alloy shell is from 10.3 to 0.23 (total Ag/Pd ratio from 5 to 1). The results from STEM and XPS analysis suggest that the thickness and the surface composition of PdAg alloy shell could be finely turned by the control of precursor concentration.

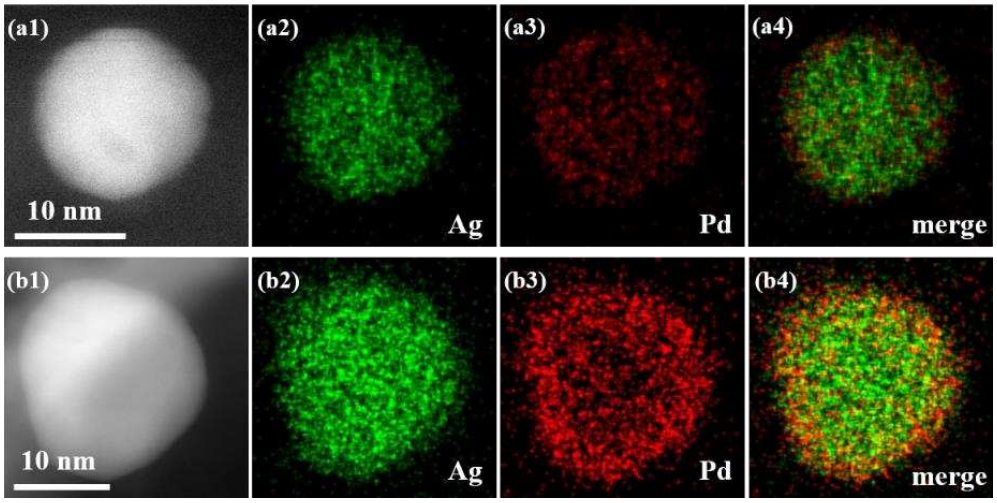

Fig. 4. HAADF-STEM images of Ag@PdAg-x with total Ag/Pd ratio of 5 (a) and 1 (b) respectively, and corresponding EDX elemental maps: Ag (green) and Pd (red).

3.2 Catalytic performance of supported Ag@PdAg core-shell catalyst.

Ethene is one of the most important chemicals which is widely used as polymerization feedstock and important intermediate in many industrial reactions. Industrially, about 0.1–1% of C_2H_2 is inevitable produced with the production of C_2H_4 from petroleum crackers, which can poison the downstream catalyst which is used for C_2H_4 polymerization and the quality of poly-ethene production [41-43]. Thus, C_2H_2 hydrogenation to C_2H_4 in excess C_2H_4 feed becomes an important industrial reaction, and it is of great economic value to promote the efficiency of this process. Improving

the selectivity and stability of catalyst for this reaction has been one of the biggest challenges in the petrochemical industry.

Table 1. The physicochemical properties of supported Ag, Pd, PdAg and Ag@PdAg catalysts.

`	Metal loading (%) [a]		d (nm) [b]	H_2 uptake	$Pd3d_{5/2}$	Dispersion	TOF (s^{-1}) [e]
	Pd	Ag		($\mu mol/mg_{Pd}$)	(eV) [c]	(%) [d]	
Ag@PdAg/LDHs	0.23	0.68	15.5	2.3	334.6	48.9	0.0190
PdAg/ LDHs	0.98	0.51	3.8	1.9	335.0	40.4	0.0099
Ag/ LDHs	-	1.01	3.2	-		-	-
Pd/ LDHs	0.97	-	3.4	3.3	335.3	-	-

[a] Determined by ICP-AES.

[b] Determined by the TEM images in Fig. S7.

[c] Recorded by XPS in Fig. 7.

[d] Calculated based on the result of H_2 uptake.

[e] TOF value estimated at 27 °C, under low conversion (<15%).

Partial hydrogenation of acetylene was then carried out over the Ag@PdAg catalyst in an ethene stream containing 1% acetylene. As comparison, supported monometallic Pd, Ag, and PdAg alloy catalysts were prepared using $NaBH_4$ as reducing agent. The metal loading of samples determined from ICP-AES is listed in Table 1, which is almost same as theoretical metal loading, as presented in Table S3. It should be noted that Pd:Ag ratio is 2:1 in PdAg alloy catalyst, which is consistent with the atomic ratio of the PdAg alloy shell on Ag@PdAg catalyst. TEM images and corresponding particle size distribution of Ag, Pd, and PdAg alloy are showed in Fig. S7, and the corresponding mean particle size is listed in Table 1. It can be seen intuitively that PdAg alloy catalyst possesses smaller nanoparticles compared with Ag@PdAg catalyst. **Fig. 5**A shows the XRD pattern of Ag, Pd, and PdAg thin films dried from colloidal sols. The peak positions of mono Pd and Ag NPs are perfect consistent with the corresponding standard pure metal. The peaks of PdAg NPs are located between those for Pd and Ag, confirming the formation of PdAg nanoalloys based on Vegard's law. The results from HAADF-STEM images and EDX elemental maps of PdAg alloy

sample, as shown in Fig. 5B, indicating that the prepared PdAg alloy possesses a homogeneous alloy structure.

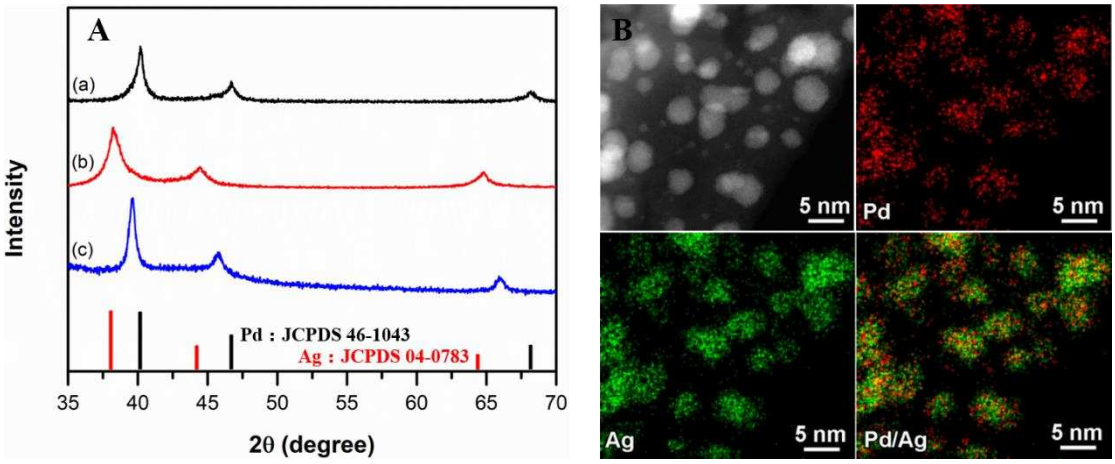

Fig. 5. (A) XRD patterns of the (a) Ag, (b) Pd, and (c) PdAg alloy thin films obtained from drying colloidal sols. (B) HAADF-STEM images and EDX elemental maps of PdAg alloy : Ag (green) and Pd (red).

In general, the addition of Ag to Pd catalyst could obviously increase the selectivity towards ethene at the expense of catalyst activity, which was accordance with the results shown in **Fig. 6**A. It can be also seen that the complete conversion of acetylene over Ag@PdAg catalyst is achieved at 100 °C, which is notably lower than that over the common PdAg alloy catalyst (100% conversion at 120 °C), indicating the activity of Ag@PdAg catalyst could be well maintained. More significantly, 97% ethene selectivity is attained at the complete elimination of acetylene over Ag@PdAg catalyst, which is 64% higher than that of the PdAg alloy at the same condition. The selectivity of ethane over Ag@PdAg catalyst is below 5% in the range from 30 to 100°C (as presented in Fig. S8). Due to its preferable activity and selectivity, Ag@PdAg catalyst shows an encouraging yield of 97% at 100 °C, which is 2.0 times and 8.1 times higher than that over PdAg alloy and Pd monometallic catalyst (Fig. 6C, D). To best of our knowledge, as presented in **Table 2**, this Ag@PdAg catalyst is one of the most selective acetylene hydrogenation catalyst under industrial evaluation conditions.

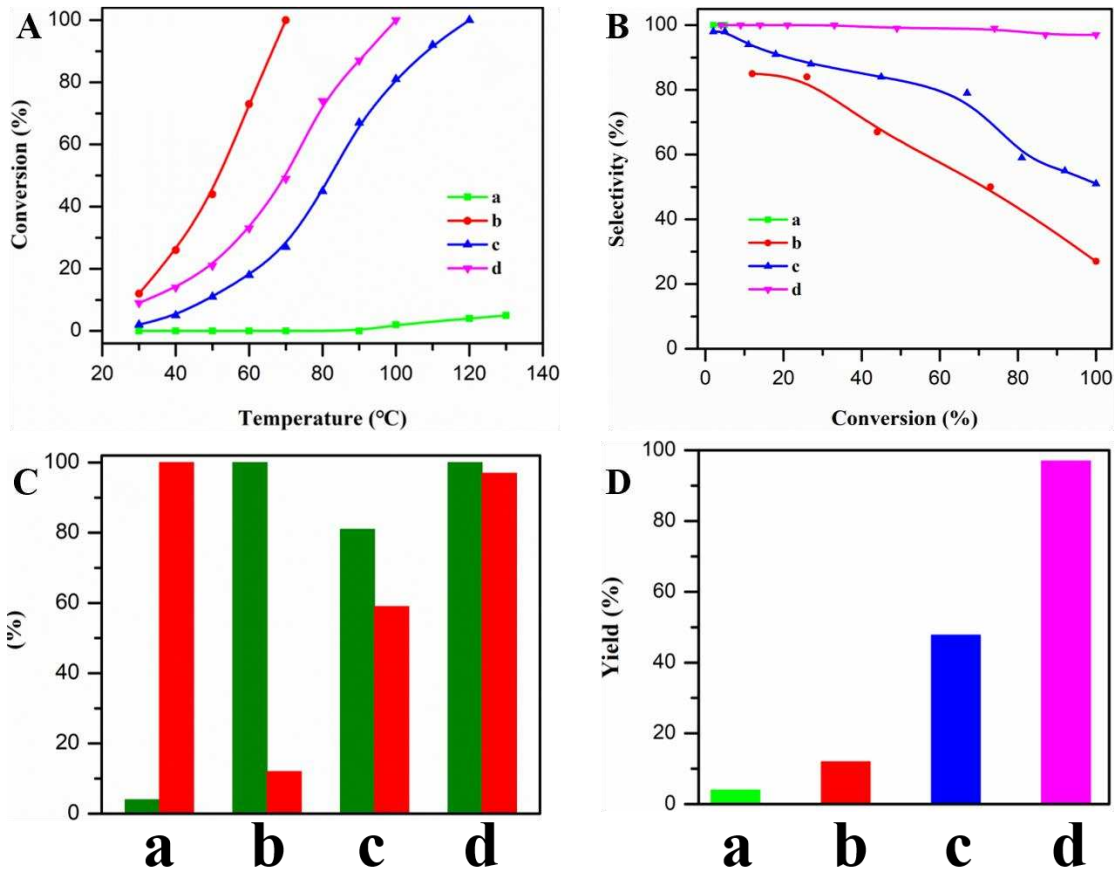

Fig. 6. Plots of (A) acetylene conversion vs. temperature, (B) ethene selectivity vs. acetylene conversion, (C) acetylene conversion and ethene selectivity at 100 °C, and (D) yield of ethene at 100 °C over LDHs supported (a) Ag, (b) Pd, (c) PdAg alloy, and (d) Ag@PdAg core-shell catalysts. The reaction temperature was varied from 30 to 130 °C with H_2: C_2H_2 ratio of ~ 2:1, space velocity (GHSV) of ca. 10,050 h^{-1} and relative pressure of 0.4 MPa.

Table 2. Comparison of catalytic performance over Pd-based catalysts.

Entry	Catalysts	Sel (%)[a]	T (°C)[b]	H_2/C_2H_2	GHSV (h^{-1})
1	Ag@PdAg/MgAl-LDH	97	100	2	10050
2	PdAg/$Mg_{0.5}Ti_{0.5}O_y$ [44]	83.8	70	2	10050
3	m-PdAg/MgAl-LDH [35]	65	90	2	8040
4	$Pd_{0.01}Ag/SiO_2$ [45]	88	160	20	60000
5	PdAg/TiO_2 [46]	40	65	5	600000
6	PdIn/Al_2O_3 [47]	72	70	3	-
7	Commercial PdAg/Al_2O_3 (BCH-20B)	51	88	2	10050
8	PdS_4/CNF [48]	94	250	1.8	60000

9	PdZn/ZnO [49]	91	150	-	-
10	$PdCu_{0.006}/SiO_2$ [50]	85	160	20	60000
11	$Pd_{0.01}Au/SiO_2$ [51]	56.4	160	20	60000

[a] Selectivity at > 99% acetylene conversion.

[b] Temperature at > 99.5% acetylen conversion.

Turnover frequency (TOF), as the intrinsic activity of the catalyst [52], is estimated and expressed as the rate of C_2H_2 consumption per number of active Pd sites on the catalyst. It is important that TOF should be based on rate measurement without the influence of mass or heat transfer. Therefore, TOF from steady-state rate measurements at low conversion (<15%) was calculated. Beyond that, the Weisz-Prater and Mears analysis were also performed for eliminating the effect of heat and mass transfer over Ag@PdAg catalyst (showed in Support Information) [53,54]. The Ag@PdAg core-shell catalyst gives a TOF of 0.0190 s^{-1}, almost two times higher than that of PdAg alloy catalyst (showed in Table 1) and that of wildly reported Pd-based catalysts under identical conditions [55-57].

Furthermore, apparent activation energy values for PdAg bimetallic catalysts with different structure are obtained by plotting ln (TOF) versus 1/T, as presented in **Fig. 7**. The Ea for C_2H_2 hydrogenation over the PdAg alloy and Ag@PdAg core-shell catalysts are 52.6 and 37.7 kJ/mol, respectively, which are located within the range of reported values (30.0-65.0 kJ/mol) for this reaction [58,59]. Moreover, it can be seen that the Ea value of Ag@PdAg catalyst is 14.9 kJ/mol lower than that of PdAg alloy catalyst, suggesting that the fabrication of Ag@PdAg core-shell catalyst could decrease the activation barrier of the reaction and then give an increase in hydrogenation activity.

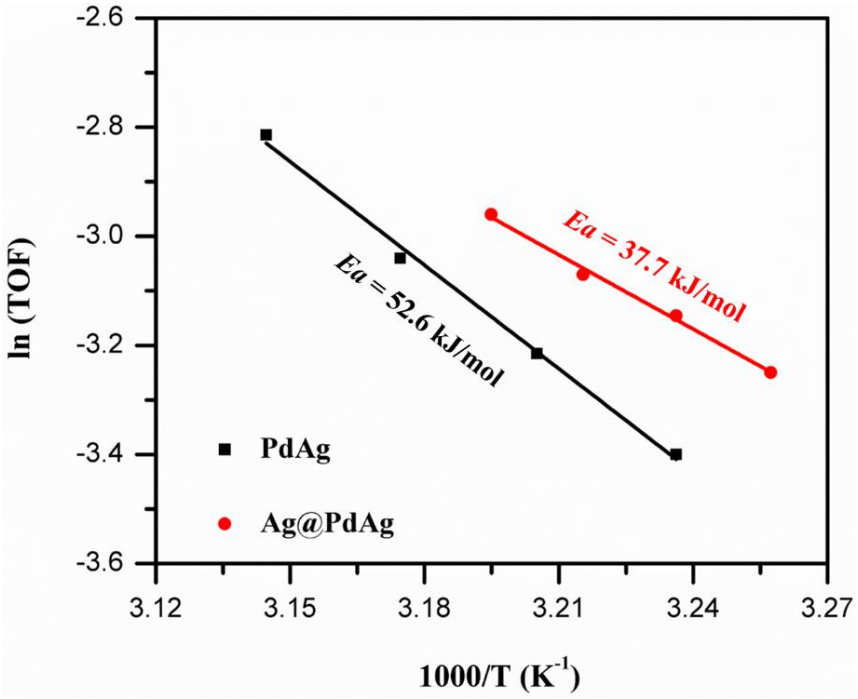

Fig. 7. Arrhenius plots for acetylene conversion over PdAg alloy and Ag@PdAg core-shell catalysts.

3.3 Insights into the structure-performance relationship.

Electronic and geometric effects, arising from the addition of a second metal, are considered to be the key factors influencing the catalytic performance of a bimetallic catalyst. Therefore, the electronic property of surface Pd of three supported Pd-based catalysts was investigated by XPS analysis. **Fig. 8**A shows a clear shift to lower binding energy in Pd 3d over PdAg alloy (0.3 eV) and Ag@PdAg core-shell catalyst (0.7 eV) compared with monometallic Pd catalyst (335.3 eV). Based on the electronegativity of the two metals, the electron would transfer from Ag to Pd within a PdAg alloy phase [60]. However, the bigger shift over Ag@PdAg suggests that an electronic modification between PdAg-alloy shell and Ag core should exist in addition to the charge transfer from Ag to Pd in the PdAg alloy shell. This modification may be caused by the lattice mismatch of core-shell heterostructure and similar surface electronic modification resulting from the interaction between core and shell metals was also found in Ag@Pd, Pd@PdCo and Pd@FePt structure in the literature [16,45,61]. Moreover, this electronic interaction declines with increasing shell thickness, as presented in Fig. S9.

Generally, the adsorption strength of reactants and products on the active metal has a significant effect on the products distribution, which is strongly influenced by the electronic structure of the active metal. In PdAg bimetallic system, it was reported that the decrease in unfilled d-states vacancies of Pd due to the presence of Ag, electron-rich Pd species, would facilitate the desorption of produced double band [45,62,63]. Therefore, in the case of Ag@PdAg catalyst, the enhanced selectivity towards ethene could be ascribed to the electron transfer from Ag to Pd in the shell as well as the electronic modification between PdAg-alloy shell and Ag core. Thus, C_2H_4-TPD over Pd, PdAg alloy, and Ag@PdAg core-shell catalysts were carried out. As showed in Fig. 8B, all three Pd-containing catalysts show one peak that can be assigned to di-σ-bonded ethene [64]. It is noted that the lower desorption temperature of ethene over Ag@PdAg (78 °C) compared to pure Pd (88 °C) and PdAg alloy (84 °C) catalyst indicates the easier desorption of ethene from the Pd surface on Ag@PdAg catalyst, which would then be favour of the increase of ethene selectivity. Besides, the same desorption temperature of C_2H_2 over PdAg and Ag@PdAg catalysts give strong support that easier desorption of C_2H_4 contributes higher selectivity of ethene (as presented in Fig. S10). As reported in the literature [45], 88% of ethene selectivity (one of the highest selectivity) was achieved when Ag/Pd ratio was close to 100, suggesting that the enhancement of ethene selectivity can be not only attributed to electronic rich Pd atoms on the surface of Pd-Ag alloy, but an electronic modification between core-shell nanostructure.

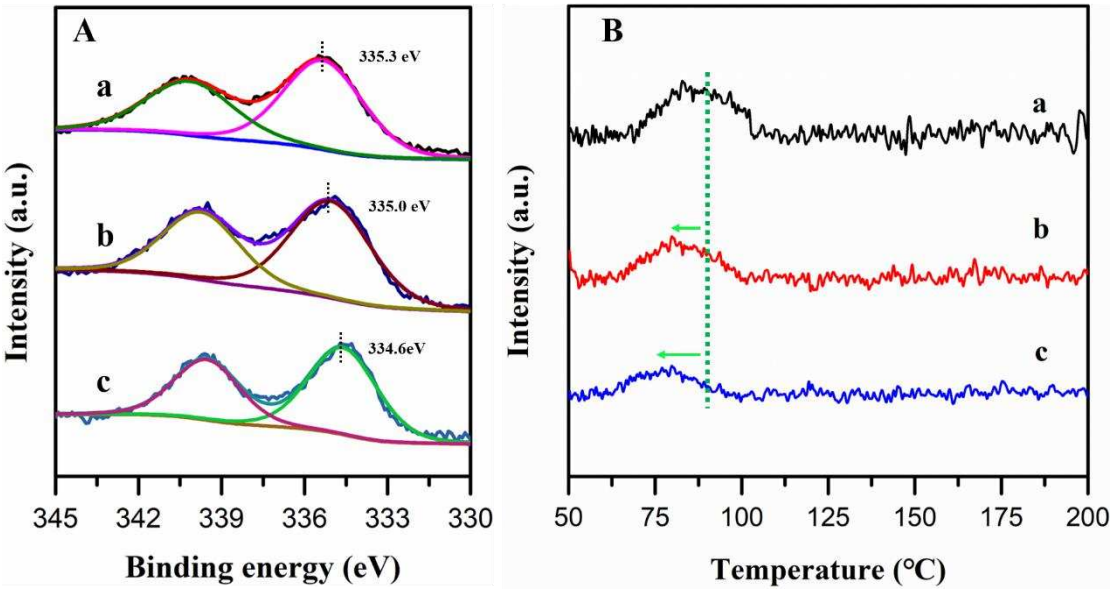

Fig. 8. (A) Pd 3d XP spectra and (B) temperature programmed desorption of C_2H_4 profiles of (a) Pd/LDHs, (b) PdAg/LDHs, and (c) Ag@PdAg/LDHs catalysts.

The distribution of Pd species on the catalyst surface was probes by FTIR via in situ CO chemisorption. It is known that CO adsorbs on Pd atom mainly in linear (2100 cm^{-1} to 2000 cm^{-1}) and multi-coordinated (between 2000 cm^{-1} to 1800 cm^{-1}) modes, while CO adsorption on Ag surface can't be detected in this condition [44,52]. **Fig. 9** shows the adsorption spectra of CO onto mono Pd, PdAg alloy and Ag@PdAg core-shell catalysts. The formation of PdAg alloy leads to a large increase in the linear adsorption in comparison with monometallic Pd catalyst, suggesting that contiguous Pd sites are separated by the addition of Ag component. On this single Pd site, the π-bonding ethene adsorption is weak, and thus contributes to the enhancement of ethene selectivity. As for Ag@PdAg sample, only a fraction of multi-coordinated adsorption mode at 1994 cm^{-1} were detected, indicating that ensembles of Pd adsorption site is almost unavailable, which further increase the ethene selectivity. Besides, there is a redshift (ca. 14 cm^{-1}) on the bimetallic Pd-Ag catalysts, with comparison to the vertical line of linear-CO on Pd catalyst, which is a result of the electronic modification between Pd and Ag and this result is consistent with XPS result.

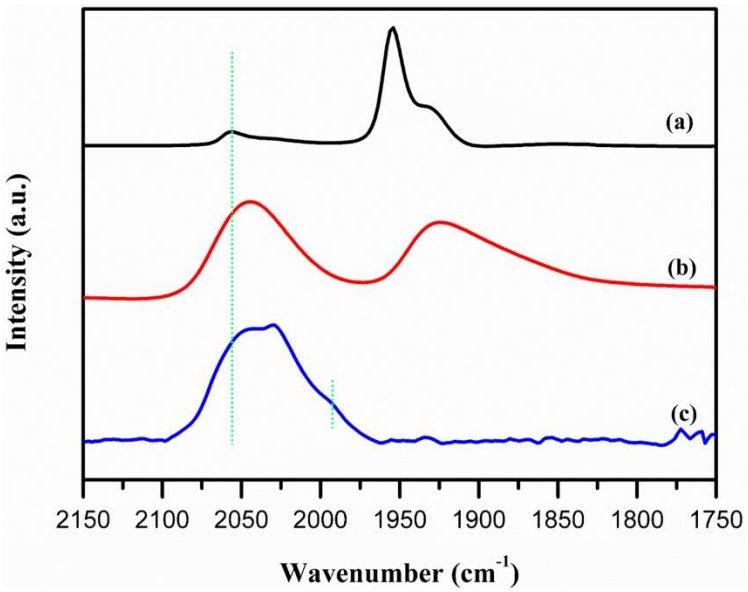

Fig. 9. In situ Fourier-transformed infrared absorption spectra of CO over (a) mono Pd, (b) PdAg alloy, and (c) Ag@PdAg core-shell catalysts.

Except for the superior selectivity, an obvious increase of TOF over Ag@PdAg catalyst was also observed. In Table 1, the dispersion of Ag@PdAg is 48.9%, which is 21% higher than that of PdAg alloy catalyst and the enrichment in Pd of the surface of Ag@PdAg could be in favour of the increase of acetylene conversion. However, TOF of core-shell catalyst is almost double than that of alloy catalyst. As shown in Fig.7, Ag@PdAg possesses a lower Ea compared with PdAg due to its special electronic modification, indicating Pd sites with high activity are formed through the fabrication of the core-shell structure. Moreover, H_2 chemisorption experiments were carried out to gain information about H_2 activation/dissociation. Ag@PdAg catalyst displays higher amount of hydrogen chemisorption compared with PdAg catalyst (presented in table 1). This preferred H_2 activation/dissociation ability over Ag@PdAg also contributes to the enhancement of acetylene conversion.

3.4 Stability of supported Ag@PdAg core-shell catalyst.

Time-on-stream test of the LDHs supported PdAg alloy, and Ag@PdAg catalysts were performed to further investigate the stability of catalysts. 100 h test over Pd-Ag bimetallic catalysts were performed at 95 ^oC with a space velocity (GHSV) of 10056 h^{-1} and H_2: C_2H_2 ratio of ~ 2. Under this condition, the initial acetylene conversion of Pd-Ag bimetallic catalysts are lower than 100%, 94% over Ag@PdAg catalyst and 75% over PdAg catalyst respectively, as shown in **Fig. 10.** The Ag@PdAg nanostructure exhibits excellent catalytic stability during a 100 h on-stream experiment. No obvious decay in selectivity of ethene is observed, while the selectivity over PdAg alloy catalyst suffered a 20.6% decrease. Similar trends were also observed towards the catalytic activity (18.7 % decline on PdAg alloy catalyst). The results of EDX-mapping (Fig. 10C, D) showed that the core-shell with alloy shell structure maintain perfectly after 100 h usage. One of the possible explanations for this preferable stability could be the structural of Ag@PdAg with a PdAg alloy surface. Due to uniform dispersion on the support and large distance between each particle, which makes them less likely to aggregate than small nanoparticles. HRTEM were taken to study the aggregation of

nanoparticles over used catalyst. As showed in Fig. S11, no aggregation and growth of the nanoparticles is seen on Ag@PdAg catalyst after 100 h usage, while 12% rise in the average size of the nanoparticles is detected over PdAg alloy catalyst. Besides the structure stability, the resistance against carbonaceous compound deposition is another measurement toward stability of catalytic performance. As a result, thermogravimetric analysis was tested to and the TG-DTA results was showed in **Fig. 11**. Generally, there are two types of coke species: unstructured carbon or trapped hydrocarbons and amorphous coke [65]. The former commonly generates on the metal site, and another forms on the acid site of support. These two types of coke can be distinguished in the temperature-programmed profile. According to the literature [66], the burning of unstructured carbon locates around 200-300 ºC and the burning of amorphous coke at higher temperature (300-400 ºC). In TG-DTA curves, the mass loss of used catalysts mainly happens under 300 ºC, indicating that the unstructured carbon species are the majority. Few coke deposition of Ag@PdAg catalyst were produced during 100 hours reaction, indicating that the preferable resistance against carbonaceous compound deposition and therefore possesses superior stability.

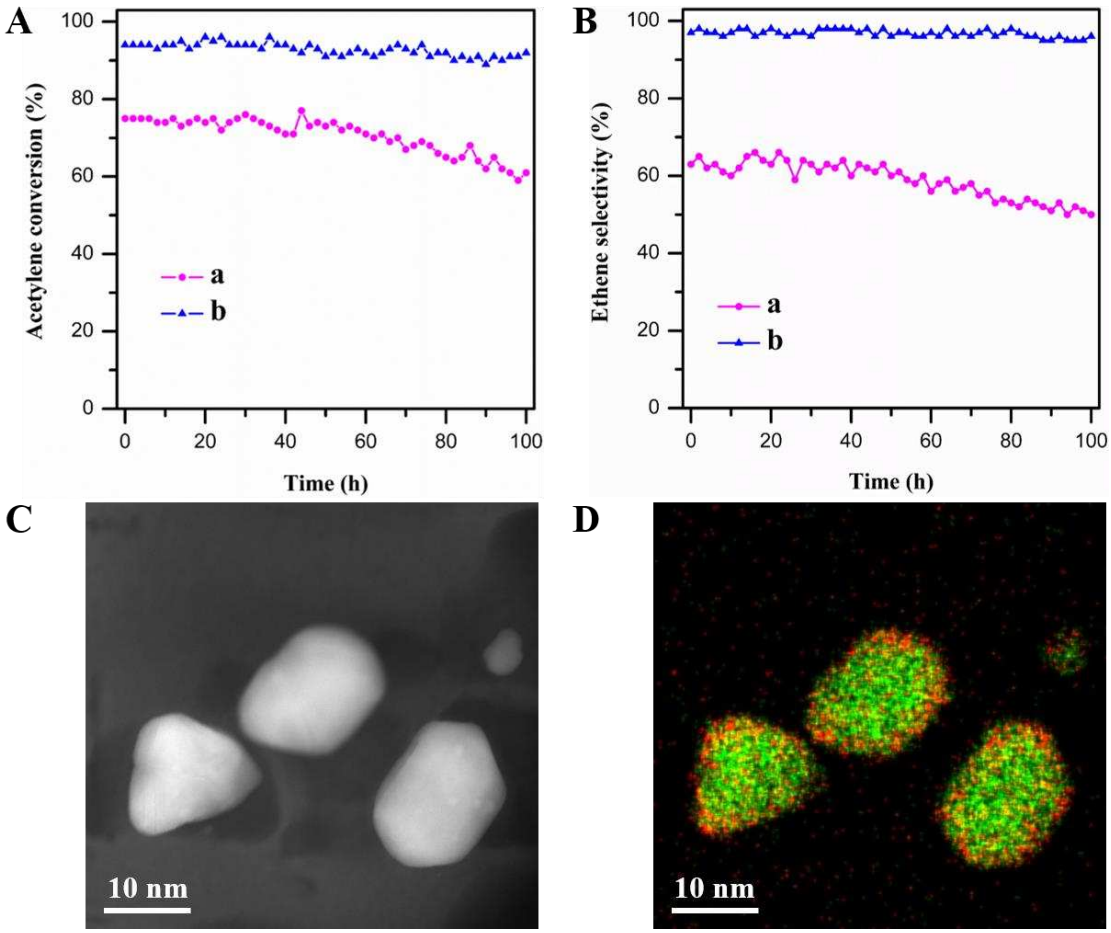

Fig. 10. Acetylene conversion (A) and ethene selectivity (B) versus reaction time at 95 °C over (a) PdAg alloy, and (b) Ag@PdAg catalysts. (C) HAADF-STEM image of Ag@PdAg catalyst after 100 h usage, (D) corresponding EDX elemental maps: Ag (green) and Pd (red).

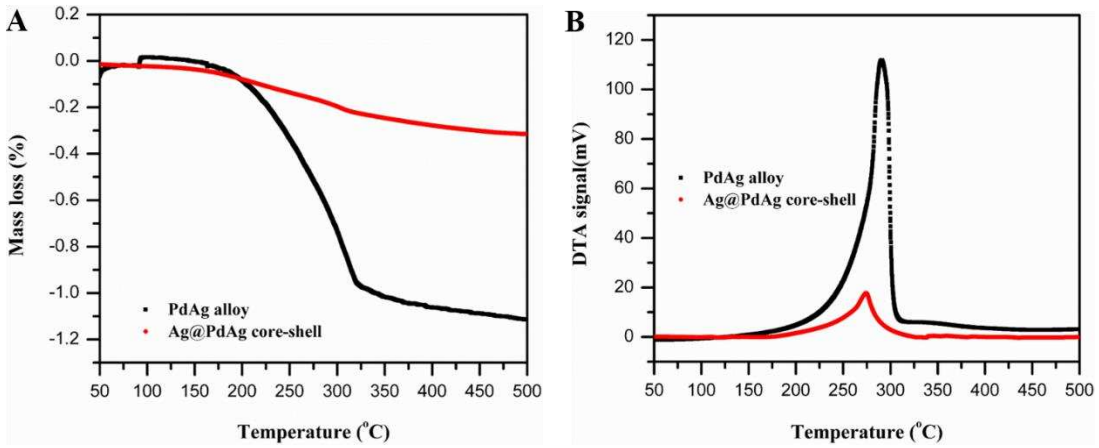

Fig. 11. (A) TG and (B) DTA curves of PdAg alloy and Ag@PdAg core-shell catalysts after 100 h usage.

4 Conclusions

We have demonstrated an effective strategy to construct Ag@PdAg core-shell nanostructure under the mild wet conditions. The STEM-EDX confirms that the nanoparticle is composed of a Ag core and an PdAg alloy shell with 3 nm. Both the relative reduction potentials and ratio of metal precursors are the key factors for the formation of the metal@alloy core-shell architecture. In partial hydrogenation of acetylene, the Ag@PdAg showed 97% ethene yield, which is 2.0 times and 8.1 times higher than PdAg alloy and Pd monometallic catalysts respectively. The enhancement of ethene selectivity can be attributed to the electronic-rich Pd atoms on the surface of PdAg alloy, and this electronic modification can be enhanced by the construction of core-shell heterostructure, which favors the desorption of ethene. The relatively lower E_a of the Ag@PdAg catalyst (37.7 kJ/mol), with comparison to alloy structure, suggests that this core-shell catalyst can decrease the activation barrier of the reaction, and thus facilitate the hydrogenation process. Moreover, this core-shell structure exhibits preferable stability and few coke were detected after 100 h reaction, with comparison to PdAg alloy catalyst. This surface alloy core-shell nanostructure with facile synthesis and unique properties could provide new strategy for the design of other important industrial catalysts.

Conflicts and interest

There are no conflicts to declare.

Acknowledgements

This work was supported by the National Key Research and Development Program of China (2016YFB0301601), the National Natural Science Foundation and the Fundamental Research Funds for the Central Universities (BUCTRC201725, JD1816).

References

[1] P. T. Anastas, M. M. Kirochhoff, Acc. Chem. Res. 2002, 35, 686.

[2] F. Zaera, Catal. Lett. 2012, 142, 501.

[3] R. Schlögl, S. B. Abd Hamid, Angew. Chem. Int. Ed. 2004, 43, 1628.

[4] F. Zaera, Chem. Soc. Rev. 2013, 42, 2746.

[5] Y. Li, Z-Y Fu, B-L Su, Adv. Funct. Mater. 2012, 22, 4634.

[6] G. A. Somorjai, Chem. Rev. 1996, 96, 1223.

[7] W. T. Yu, M. D. Porosoff, J. G. Chen, Chem. Rev. 2012, 112, 5780.

[8] D. M. Alonso, S. G. Wettstein, J. A. Dumesic, Chem. Soc. Rev. 2012, 41, 8075.

[9] M. Sankar, N. Dimitratos, P. J. Miedziak, P. P. Wells, C. J. Kiely, G. J. Hutchings, Chem. Soc. Rev, 2012, 41, 8099.

[10] D. S. Wang, Y. D. Li, J. Am. Chem. Soc, 2010, 132, 6280.

[11] Y. J. Huang, X. C. Zhou, M. Yin, C. P. Liu, W. Xing, Chem. Mater, 2010, 22, 5122.

[12] S. Y. Song, K. Li, J. Pan, F. Wang, X. Wang, H. J. Zhang, Adv. Mater. 2017, 160, 5332.

[13] X. Wang, M. Vara, M. Luo, H. W. Huang, Y. N. Xia, J. Am. Chem. Soc. 2015, 137, 15036.

[14] J-L Blin, A. Léonard, Z-Y Yuan, L. Gigot, A. Vantomme, A. K. Cheetham, B-L Su, Angew. Chem. Int. Ed. 2003, 115, 2978.

[15] C. Koenigsmann, A. C. Santulli, K. P. Gong, M. B. Vukmirovic, W. P. Zhou, S. S. Wong, R. R. Adzic, J. Am. Chem. Soc. 2011, 133, 9783.

[16] K. Tedsree, T. Li, S. Jones, K. M. Kerry Yu, S. Chi E. Tsang, Nature Nanotechnology 2011, 6, 302.

[17] X. M. Sun, Y. D. Li, Angew. Chem. Int. Ed. 2004, 43, 597.

[18] R. G. Chaudhuri, S. Paria, Chem. Rev, 2012, 112, 2373.

[19] P. Reiss, M. Protière, L. Li, Small, 2009, 5, 154.

[20] F. Wang, R. R. Deng, J. Wang, Q. Q. Wang, X. G. Liu, Nature Materials, 2011, 10, 968.

[21] L. F. Cui, R. Ruffo, C. K. Chan, H. L. Peng, Y. Cui, Nano Lett. 2009, 9, 491.

[22] Z. Q. Li, L. Y. Zhang, X. L. Ge, C. X. Li, S. H. Dong, C. X. Wang, L. W. Yin, Nano Energy, 2017, 32, 494.

[23] L. S. Xie, F. L. Qu, Z. Liu, X. Ren, S. Hao, R. X. Ge, G. Du, A. M. Asiri, X. P. Sun, L. Chen, J. Mater. Chem. A, 2017, 5, 7806.

[24] S. Assali, A. Dijkstra, A. Li, S. Koelling, M. A. Verheijen, L. Gagliano, N. von den Driesch, D. Buca, P. M. Koenraad, J. E. M. Haverkort, E. P. A. M. Bakkers, Nano Lett. 2017, 17, 1538.

[25] Z. M. Peng, H. J. You, H. Yang, Adv. Funct. Mater. 2010, 50, 3734.

[26] A. K. Singh, Q. Xu, ChemCatChem, 2013, 5, 652.

[27] Y. W. Lee, M. J. Kim, S. W. Kang, S. W. Han, Angew. Chem. 2011, 123, 3528.

[28] V. Mazumder, M. F. Chi, K. L. More, S. H. Sun, J. Am. Chem. Soc, 2010, 132, 7848.

[29] M. Meng, Z. C. Fang, C. Zhang, C. Ma, J. Zeng, Nano Lett. 2016, 16, 3036.

[30] Y. J. Kang, J. S. Snyder, M. F. Chi, D. G. Li, V. R. Stamenkovic, Nano Lett. 2014, 14, 6361.

[31] C. H. Cui, L. Gan, H. H. Li, S. H. YU, M. Heggen, P. Strasser, Nano Lett. 2012, 12, 5885.

[32] C. H. Cui, L. Gan, M. Heggen, S. Rudi, P. Strasser, Nat. Mater. 2013, 12, 765.

[33] J. T. Feng, Y. F. He, Y. N. Liu, Y. Y. Du, D. Q. Li, Chem. Soc. Rev., 2015, 44, 5291.

[34] F. Cavani, F. Trifirü, A. Vaccari, Catal. Today, 1991, 11, 173.

[35] Y. F. He, Y. N. Liu, P. F. Yang, Y. Y. Du, J. T. Feng, X. Z. Cao, J. Yang, D. Q. Li, J. Catal., 2015, 330, 362.

[36] M. Sobota, I. Nikiforidis, M. Amende, B. S. Zanón, T. Staudt, O. Höfert, Y. Lykhach, C. Papp, W. Hieringer, M. Laurin, D. Assenbaum, P. Wasserscheid, H-P Steinrück, A. Görling, J. Libuda, Chem. Eur. J. 2011, 17, 11542.

[37] L. Q. Liu, F. Zhou, L. G. Wang, X. J. Qi, F. Shi, Y. Q. Deng, J. Catal. 2010, 274, 1.

[38] J. Xu, T. White, P. Li, C. H. He, J. G. Yu, W. K. Yuan, Y-F Han, J. Am. Chem. Soc. 2010, 132, 10398.

[39] H. L. Skriver, N. M. Rosengaard, Phys. Rev. B, 1992, 46, 7157.

[40] M. Li, D. Weng, X. D. Wu, B. Wang, Catal. Today, 2013, 201, 19.

[41] G. C. Bond, P. B. Wells, J. Catal. 1966, 5, 65.

[42] A. N. R. Bos, K. R. Westerterp, Chem. Eng. Progress, 1993, 32, 1.

[43] A. Borodzinski, G. C. Bond, Catal. Rev. 2006, 48, 91.

[44] Y. N. Liu, J. Y. Zhao, J. T. Feng, T. Wu, D. Q. Li, J. Catal., 2017, 348, 135.

[45] G. X. Pei, X. Y. Liu, A. Q. Wang, A. F. Lee, M. A. Isaacs, L. Li, X. L. Pan, X. F. Yang, X. D. Wang, Z. J. Tai, K. Wilson, T. Zhang, ACS Catal., 2015, 5, 3717.

[46] S. Riyapan, Y. Y. Zhang, A. Wongkaew, J. Panpranot, Catal. Sci. Technol., 2016, 6, 5608.

[47] Y. Q. Cao, Z. J. Sui, Y. Zhu, X. G. Zhou, D. Chen, ACS Catal., 2017, 7, 7835.

[48] A.J. McCue, A. Guerrero-Ruiz, I. Rodríguez-Ramos, J. A. Anderson, J. Catal., 2016, 340, 10.

[49] H. R. Zhou, X. F. Yang, T. Zhang, ACS Catal., 2016, 5, 1054.

[50] G. X. Pei, X. Y. Liu, T. Zhang, ACS Catal., 2017, 7, 1491.

[51] F. R. Lucci, M. T. Darby, E. C. Sykes, 2016, J. Phys. Chem. Lett., 2016, 7, 480.

[52] Y. F. He, J. T. Feng, Y. Y. Du, D. Q. Li, ACS Catal., 2012, 2, 1703.

[53] P. B. Weisz, C. D. Prater, Adv. Catal., 1954, 6, 143.

[54] S. T. Oyama, X. Zhang, J. Lu, Y. Gud, T. Fujitani, J. Catal., 2008, 257, 1.

[55] F. -M. McKenna, J. A. Anderson. J. Catal., 2011, 281, 231.

[56] D. E. Mears, Ind. Eng. Chem. Process. Des. Dev., 1971, 10, 541.

[57] W. -J. Kim, J. H. Kang, I. Y. Ahn, S. H. Moon, J. Catal., 2004, 226, 226.

[58] H. Molero, B. F. Bartlett, W. T. Tysoe, J. Catal., 1999, 181, 49.

[59] D. Duca, F. Arena, A. Parmaliana, G. Deganello, Appl. Catal. A, 1998, 172, 207.

[60] D. E. Mears, Ind. Eng. Chem. Process. Des. Dev., 1971, 10, 541.

[61] D. A. Slanac, W. G. Hardin, K. P. Johnton, K. J. Stevenson. J. Am. Chem. Soc. 2012, 134, 9812

[62] A. J. McCue, C. J. Mcritchie, A. M. Shepherd, J. A. Anderson, J. Catal. 2014, 319, 127.

[63] J. Prinz, C. A. Pignedoli, Q. S. Stöckl, M. Armbrüster, H. Brune, O. Gröning, R. Widmer, D.Passerone, J. Am. Chem. Soc. 2014, 133, 11792.

[64] A. M. Doyle, S. K. Shaikhutdinov, H. -J. Freund, Angew. Chem. Int. Ed., 2005, 44, 629.

[65] C. Ma, Y. Y. Du, J. T. Feng, X. Z. Cao, J. Yang, D. Q. Li, J. Catal., 2014, 317, 263.

[66] Y. Azizi, C. Petit, V. Pitchon, J. Catal., 2008, 256, 338.